



## DISPERSION FORCES AND HAMAKER CONSTANTS FOR INTERGRANULAR FILMS IN SILICON NITRIDE FROM SPATIALLY RESOLVED-VALENCE ELECTRON ENERGY LOSS SPECTRUM IMAGING

R. H. FRENCH<sup>1</sup>, H. MÜLLEJANS<sup>2†</sup>, D. J. JONES<sup>1</sup>, G. DUSCHER<sup>2</sup>,  
R. M. CANNON<sup>3</sup> and M. RÜHLE<sup>2</sup>

<sup>1</sup>DuPont Co. Central Research, E356-384 Experimental Station, Wilmington, DE 19880, U.S.A., <sup>2</sup>Max-Planck-Institut für Metallforschung, Seestr. 92, D-70174 Stuttgart, Germany and <sup>3</sup>Lawrence Berkeley Lab., Hearst Mining Bldg. University of California, Berkeley, CA 94720, U.S.A.

**Abstract**—The van der Waals (vdW) dispersion forces represent one of the fundamental long range interfacial and surface forces in materials. The dispersion forces, for a set of materials in close proximity, arise from the electronic structure of the materials wherein the electrons in interatomic bonds acting as oscillating dipoles exhibit an attractive interaction energy. These vdW dispersion forces, represented by a proportionality constant, the full spectral Hamaker constant ( $A$ ), can be calculated directly from optical property based electronic structure spectra such as the interband transition strength ( $J_{cv}$ ) using the Lifshitz theory.  $\text{Si}_3\text{N}_4$  exhibits equilibrium intergranular films (IGFs) whose thickness is determined by a force balance where the contribution of the van der Waals dispersion force is dictated by the IGF chemistry. Using spatially resolved-valence electron energy loss (SR-VEEL) spectroscopy in the STEM with a 0.6 nm probe permits the *in situ* determination of vdW forces on the IGFs in viscous sintered polycrystalline systems. In addition local variations in IGF chemistry and dispersion forces throughout the microstructure of individual silicon nitride samples can be determined using these methods. From multiplexed zero loss/plasmon loss optimized SR-VEEL spectra across IGFs with subsequent single scattering deconvolution, Kramers Kronig analysis and London dispersion analysis, the index of refraction and Hamaker constants can be determined. The method proved to be accurate and reproducible with comparison to VUV measurements for the bulk materials and repeated measurements on numerous individual IGFs. For these optimized  $\text{Si}_3\text{N}_4$  materials, the dispersion forces varied over a range from 2 to 12 zJ. These showed standard deviations on the order of 1 zJ for systems with IGFs. Additional systematic errors can not be excluded. Local variations in Hamaker constants within the microstructure of a single sample correlate to the distribution of IGF thicknesses observed, i.e. the thickness varies inversely with Hamaker constant. The technique of measuring Hamaker constants *in situ* represents an important new tool for dispersion force and wetting studies. For the first time it is observed that the thickness of the IGF scales with the local Hamaker constant of the investigated grain boundary region. © 1998 Acta Metallurgica Inc.

### 1. INTRODUCTION

It is widely accepted that oxide rich intergranular films (IGFs) exist along most interfaces in  $\text{Si}_3\text{N}_4$ -based materials [1, 2]. In addition IGFs are widely found in many other ceramic systems including  $\alpha$ - $\text{Al}_2\text{O}_3$  [3–5],  $\text{ZrO}_2$  [6],  $\text{ZnO}$  [7, 8], titanates [9] as well as in  $\text{AlN}$  [10]. Similar IGFs have also been reported to play a critical role in the properties of thick film (or “chip”) resistors based on ruthenate particles [11]. Fluoride rich IGFs have also been seen in  $\text{MgAl}_2\text{O}_4$  spinel [12]. The IGFs have often been regarded as wetting liquids which aid densification during liquid phase sintering processes. From a fundamental point of view it is more fruitful to recognize that these liquids are multilayer adsorbates which do not fully wet the grain boundaries. The IGFs are comprised of the constituents

of the adjacent intergranular pockets, however the composition of the IGFs and the glass in the intergranular pockets may not necessarily be the same. It is also not expected that the composition is uniform across the IGF.

For an understanding of the interaction forces across the grain boundary and their energetics it is desirable to measure the thicknesses as well as the composition of the IGFs. Recently Kleebe *et al.* [13, 14], using high resolution electron microscopy (HREM), have shown that typically the thickness is uniform within the observed accuracy of  $\pm 0.1$  nm for a given material of a specific composition. They have argued that since it varies from material to material it must depend upon composition and more specifically on chemical activity. However until recently the only clear trend to emerge experimentally has been a complex dependence upon CaO content from the  $\text{Ca-SiO}_2\text{-Si}_3\text{N}_4$  materials of Tanaka, and as yet no compelling theory has been shown to predict other trends. In

<sup>†</sup>Now at: Institute for Advanced Materials, Joint Research Centre, European Commission, PO Box 2, NL-1755 ZG Petten, The Netherlands.

addition, Kleebe has claimed, based upon limited and somewhat inconsistent data for confirmation, that the thickness does not depend on the volume fraction of glass present, as long as the chemical activities are held constant. These findings can be summarized for undoped  $\text{SiO}_2\text{-Si}_3\text{N}_4$  materials, Ca doped  $\text{SiO}_2\text{-Si}_3\text{N}_4$  materials and  $\text{RE}_2\text{O}_3$  doped  $\text{Si}_3\text{N}_4$  materials to serve as a background for the materials studied in the current work.

The determination of the composition of the IGF and the measurement of the variation of the composition by analytical electron microscopy is much more difficult. Gu *et al.* [15–17] suggest techniques for measuring the average composition of the IGF, however variations across the IGF cannot be determined. Pan *et al.* [18] have shown that for undoped  $\text{SiO}_2\text{-Si}_3\text{N}_4$  materials coming from various sources the thickness of the IGF is invariant at 1.05 nm for volume fractions of  $\text{SiO}_2$  varying between 4 and 17 wt%.

Adding Ca to the undoped  $\text{SiO}_2\text{-Si}_3\text{N}_4$  material [19,20] caused the IGF thickness of these otherwise pure materials to decrease down to 0.7 nm (for an average addition of 80 ppm Ca) and then to increase up to 1.45 nm, with increasing Ca levels. The Ca- $\text{SiO}_2\text{-Si}_3\text{N}_4$  sample studied in this work was prepared with 450 ppm Ca and exhibited 1.45 nm IGF thicknesses. It was proposed that the resulting thickness is an interplay between the attractive vdW forces and the repulsive steric forces and forces caused by electric double layers [21].

For  $\text{Si}_3\text{N}_4$  materials with a significant addition of rare earth modifiers, there is a strong systematic increase in IGF thickness with ionic radius for trivalent rare earth modifiers, and two sets (polycrystals and quasidisordered particles) of such samples yield an even stronger affirmation of the independence of the thickness on volume fraction given that the chemical activities are held constant [22]. As suggested by Clarke [21,23] and shown by Tanaka [19,20] the equilibrium IGF thickness results from the attractive van der Waals forces and the repulsive steric and double layer forces. All these forces depend on the composition of the IGF. For the vdW forces the dependence on composition is described by the Hamaker constant which is the proportionality factor for the vdW forces caused by the transient induced dipoles associated with interatomic bonds. It is most desirable to determine the Hamaker constant,  $A$ , of the IGF, but there exists no direct way of measurement. However, as shown by French *et al.* [24], an indirect way of determining  $A$  is by determining the electronic structure and interband transitions of  $\text{Si}_3\text{N}_4$  and the IGF and then calculating the Hamaker constant. In this paper it will be shown that the “local” Hamaker constant can be evaluated from spatially-resolved valence electron energy loss spectroscopy (SR-VEELS). In the next section the basis of Hamaker constant determination is summarized, before the

experimental results are reported and evaluated. Technical details of the multiplexed zero loss, plasmon loss optimized spectrum images are given in Appendix A. A discussion of the results concludes the paper.

## 2. EVALUATION OF THE HAMAKER CONSTANT FROM *IN SITU* SPECTROSCOPY

The vdW attraction forces, as given by the Hamaker constant  $A$ , arise from transient induced dipoles associated with interatomic bonds. The Hamaker constant [24] can be calculated directly from the interfacial electronic structure of the IGF using Kramers Kronig analysis of the interband transition strength  $J_{cv}(\omega)$  to yield  $\epsilon_2(\xi)$  for the phases present, producing full spectral values for the configuration-dependent Hamaker constants of the vdW forces. Therefore the problem reduces to determining the electronic structure and interband transitions of silicon nitride and the IGFs, and then the Hamaker constants of the vdW dispersion forces can be calculated. There have been previous comparisons of these full spectral Hamaker constants with those derived from force measurements [25] and other physical property based Hamaker constant estimation schemes [26]. The full spectral method is the most direct implementation of Lifshitz’s original quantum field theory approach to dispersion forces.

There have been numerous studies of the electronic structure of  $\text{Si}_3\text{N}_4$  including the local density approximation (LDA) orthogonalized linear combination of atomic orbitals (OLCAO) band structure calculations of Ren and Ching [27], Robertson’s bond orbital study [28], and the empirical electronic structure calculations of Sokel [29]. Of interest to the present focus on polycrystalline  $\text{Si}_3\text{N}_4$  as a structural ceramic exhibiting thin IGFs, is the work of Ching *et al.* on a silicon oxynitride composition  $\text{Si}_2\text{N}_2\text{O}$  [30,31]. In addition, driven by the use of silicon nitride films in electronics [32], there have been many studies of the visible and UV optical properties of silicon nitride [33], silicon-oxynitride [34] and silicon-fluoronitride films [35]. Recently there has been an extensive study of silicon nitride thin film optical properties up to 9.5 eV reported by Petalas *et al.* [36].

For full spectral Hamaker constant calculations, one requires an optical property based perspective of the interband transitions and optical properties of the materials [37]. Either vacuum ultraviolet (VUV) spectroscopy [38] (2–44 eV) coupled with spectroscopic ellipsometry [39] (1.5–6.65 eV), or valence electron energy loss (VEEL) spectroscopy [40] can be used to determine the interband transition strength  $J_{cv}$ , which is algebraically related to the dielectric function  $\epsilon(E)$ :

$$J_{cv}(E) = \frac{m_0^2 E^2}{e^2 \hbar^2 8\pi^2} (\epsilon_2(E) + i\epsilon_1(E)) \quad (1)$$

where  $m_0$  and  $e$  are the mass and the charge of the electron,  $E$  is the energy and  $\hbar$  Planck's constant.  $J_{cv}(E)$  has units of density, but for computational convenience we take the prefactor  $m_0^2 e^{-2} \hbar^{-2}$  whose value in cgs-units is  $8.289 \cdot 10^{-6} \text{ g cm}^{-3} \text{ eV}^{-2}$ , as unity and therefore the  $J_{cv}(E)$  spectra plotted in this paper have units of  $\text{eV}^2$ .

Electron energy-loss spectroscopy in the transmission electron microscope (TEM) has been used to assess a variety of information on the specimen such as chemical composition, partial density of states in the conduction band, pair distribution functions and the dielectric function [41]. The TEM offers a typical beam diameter of 10 nm for analysis modes, therefore single grains in polycrystalline materials can easily be selected. In a dedicated STEM the primary beam diameter is well below 1 nm and therefore one is able to investigate small particles and defects such as internal interfaces (e.g. grain boundaries) directly. The low energy, or valence, loss part of the spectrum (up to about 50 eV) and its relation to the dielectric theory of materials has been extensively studied by Howie and his group [42–44]. For bulk material they extracted the dielectric function from VEEL spectra and compared them to the data determined by optical spectroscopy. In general they found good agreement. For specific specimen geometries such as interfaces (surfaces and internal interfaces), small particles and holes in bulk material they then calculated the expected VEEL spectrum from dielectric theory. The agreement with experiment was again good. In their analysis they did not proceed, however, to determine the electronic structure (interband transition strength) and other materials properties such as Hamaker constants, as will be done in this paper.

Traditionally (V)EEL spectroscopy has been done by taking single measurements for various positions of the primary electron beam on the specimen. More recently automatic beam positioning and synchronized spectrum acquisition has been implemented [45,46]. This method is called “spectrum imaging” and we used a similar system but with additional facilities, which will be described in the appendix. This system offers full two-dimensional mapping, but for the evaluation of interfaces in this paper only one dimensional scans (profiles) were required.

The determination of interface electronic structure from spatially resolved-valence electron energy loss (SR-VEEL) spectroscopy has been demonstrated for a particular  $\Sigma 11$  grain boundary in alumina [40]. First results for *in situ* determination of Hamaker constants has also been published [47]. The work presented here extends on those previous

investigations. The aim is to determine the dependence of Hamaker constants on IGF chemistry.

### 3. EXPERIMENTAL METHODS AND RESULTS

#### 3.1. Samples

The samples studied in the current work fall in to two classes, those based on lanthanide (R) glasses of the type R–Si–Al–O–N glass compositions and simple silicate glass compositions containing calcium of the type Ca–Si–O–N. The lanthanide glass samples used either yttrium aluminum (herein referred to as YAl) or lanthanum aluminum (LaAl) doped silicon oxynitride glass. These were prepared by making samples of nominal composition 30 equiv% R, 30 equiv% Al, 40 equiv% Si, 78 equiv% O, and 22 equiv% N using as source materials Ube-SN-E10 and Ube-SN-E03 silicon nitride [48], Aerosil silica by Degussa, Alumalux-49SG alumina by Alcoa and fine grade lanthanides from H. C. Starck. These were gas pressure sintered for 60 min at 1840°C at a maximum pressure of 10 MPa  $\text{N}_2$  with a cooling rate of  $\sim 28^\circ\text{C}$  per minute to 1000°C. For the vacuum ultraviolet spectroscopy of the YAl glass composition, and additional sample of the bulk Y–Al–Si–O–N glass was made to permit a bulk sample of this glass to be studied using VUV spectroscopy. The thermochemistry of these lanthanide glass silicon nitride samples is discussed in detail by Krämer [49].

The calcium doped silicate glass silicon nitride samples were made by Tanaka [19,20]. A slurry of  $\text{Si}_3\text{N}_4$  and  $\text{Ca}(\text{NO}_3)_2 + \text{H}_2\text{O}$  was ultrasonically mixed, dried and compacted and finally densified by hot isostatic pressing at 1950°C for 1 h under 170 MPa. The oxygen content was 1.3 wt% and the Ca concentration was 450 ppm with no other cation impurities detected.

#### 3.2. VUV spectroscopy

VUV spectroscopy and spectroscopic ellipsometry were performed on bulk samples of the YAl– $\text{Si}_3\text{N}_4$  material, along with the Y–Al–Si–O–N bulk glass sample whose composition is expected to be similar to the triple point composition in equilibrium with  $\text{Si}_3\text{N}_4$  at the sintering temperature. From spectroscopic ellipsometry we determined the complex index of refraction of these two samples (Fig. 1), which show that the real index of this silicon nitride, extrapolated to zero energy, is 1.97 while that of the Y–Al–Si–O–N bulk glass is 1.78. The index of  $\text{Si}_3\text{N}_4$  will be used in the index sum rule applied in the analysis of SR-VEEL spectra to scale the  $y$ -axis of the single scattering energy loss function.

Kramers Kronig analysis [50,51] of the VUV spectra [52] yields the interband transitions of the YAl– $\text{Si}_3\text{N}_4$  material and the Y–Al–Si–O–N bulk glass (Fig. 2(a)). Use of another Kramers Kronig

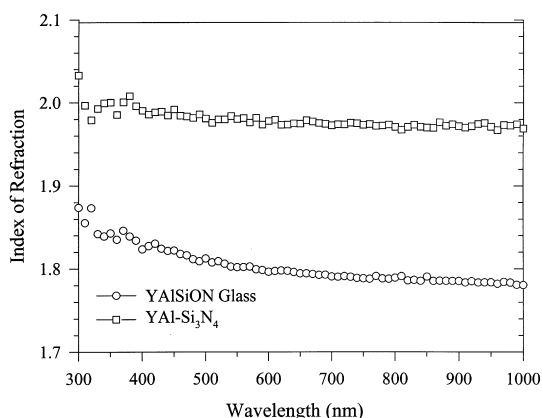


Fig. 1. The spectral dependence of the index of refraction of the YAl-Si<sub>3</sub>N<sub>4</sub> sample and the bulk Y-Al-Si-O-N glass sample determined using spectroscopic ellipsometry. These show the long wavelength limiting values for the index of 1.97 for YAl-Si<sub>3</sub>N<sub>4</sub> and 1.78 for bulk Y-Al-Si-O-N glass.

transform of the Interband transition strength produces the London dispersion spectra for these two materials (Fig. 2(b)). From these London dispersion spectra the Hamaker constant for [Y-

AlSi<sub>3</sub>N<sub>4</sub>|Vacuum|Y-AlSi<sub>3</sub>N<sub>4</sub>] configuration was determined to be 192 zJ ( $10^{-21}$  J) while the Hamaker constant for [Y-AlSi<sub>3</sub>N<sub>4</sub>|Y-Al-Si-O-N bulk glass|Y-AlSi<sub>3</sub>N<sub>4</sub>] configuration is 9.3 zJ. These values will serve as VUV reference values for comparison to vacuum and IGF Hamaker constants determined from SR-VEEL spectrum images.

### 3.3. Microscopy

SR-VEEL spectra were acquired on the Si<sub>3</sub>N<sub>4</sub> samples with a Gatan 666 parallel EEL spectroscopy system fitted to a Vacuum Generators HB501 dedicated scanning transmission electron microscope (STEM) operated at 100 keV. The high-resolution version of the objective lens focused the incident beam into a spot of 0.6 nm diameter with a convergence semi-angle of 10 mrad. The collection semi-angle of the spectrometer was 13 mrad and the energy resolution of the whole system was better than 0.7 eV as determined from the full-width-half-maximum of the zero-loss peak. The energy dispersion was 0.1 eV/channel and each spectrum covered the energy-loss range from -20 eV to 80 eV. Single spectra were acquired by the GATAN EI/P software [53], whereas the multiplexed spectrum

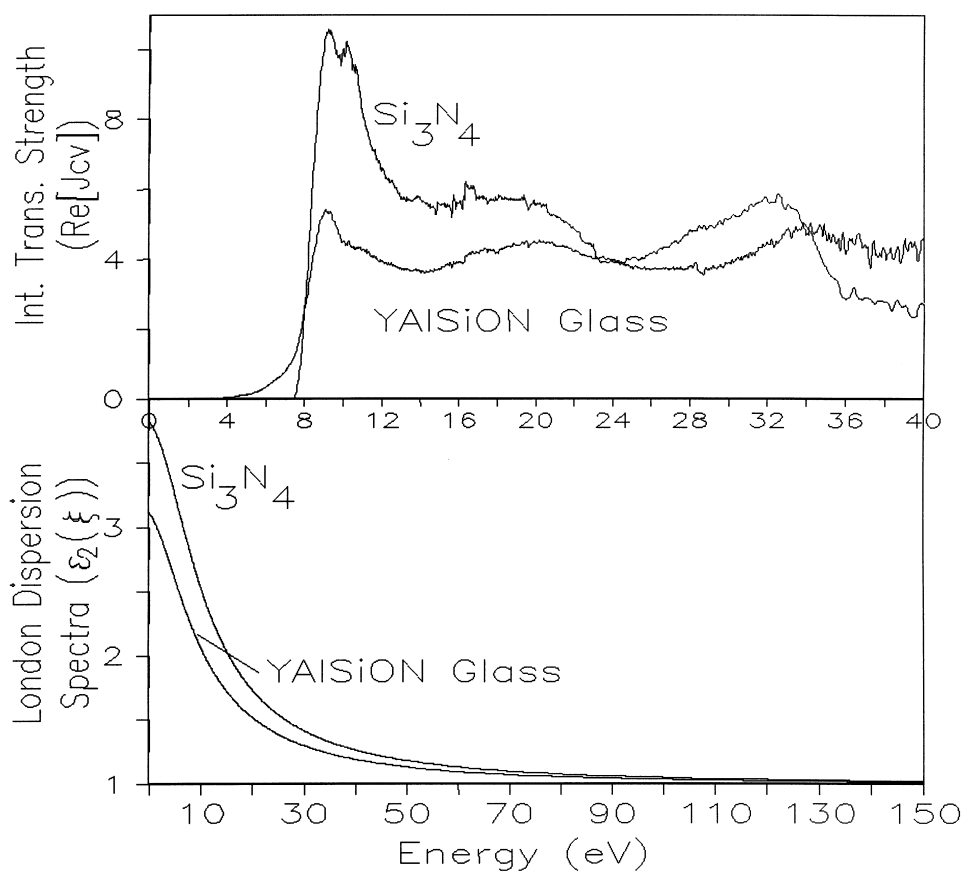


Fig. 2. Interband transition strengths ( $\text{Re}[J_{cv}]$ ) and London dispersion spectra for the YAl-Si<sub>3</sub>N<sub>4</sub> sample and the Y-Al-Si-O-N bulk glass sample determined by VUV spectroscopy.

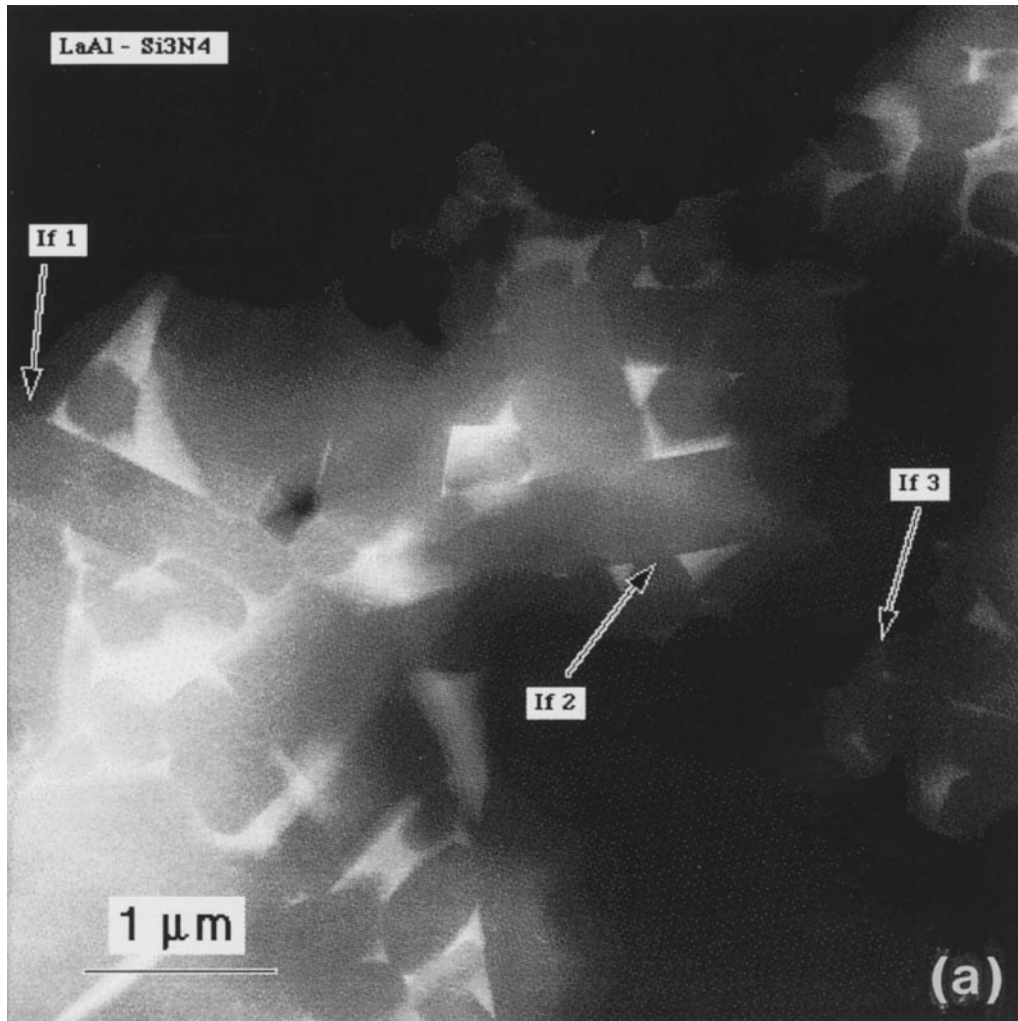


Fig. 3(a)—Caption overleaf.

images were acquired and analyzed as discussed in the Appendix. Figure 3 shows the microstructure and the four interfaces analyzed in the LaAl-Si<sub>3</sub>N<sub>4</sub> material.

#### 3.4. Full spectral Hamaker constant calculation

The interband transition strength spectrum images can be determined from the analysis of SR-VEEL spectra as discussed in Appendix A. The next step is to calculate the magnitude of dispersion force or interaction energy, as given by the non-retarded Hamaker constant [54]  $A$ , (as defined in equation (2))

$$A = -12\pi L^2 E \quad (2)$$

†Our equation (3) is identical to Ninham and Parsegian's equation (15), except that  $L^2$  in their equation defines a unit area whereas we define  $E$  per unit area so the  $L^2$  does not arise in equation (3). We use the symbol  $L$  to represent the film thickness.

which is the configuration-dependent scaling coefficient for the van der Waals interaction energy for two materials #1 and #3 separated by an intervening material #2 defined by Fig. 4. Here  $L$  is the thickness of the intervening film while  $E$  is the van der Waals interaction energy. As reported here Hamaker constants are in units of zepto-joules ( $\text{zJ} = 10^{-21} \text{ J}$ ).

To calculate the Hamaker constant using the full spectral method [24] it is necessary to perform another Kramers Kronig-based integral transform so as to produce the London dispersion spectrum of the interband transitions for the two grains and the intervening film. Following Lifshitz [55], Dzyaloshinskii, Lifshitz and Pitaevskii [56], Ninham and Parsegian [57]†, and Hough and White [58], we proceed to use the London dispersion transform

$$\varepsilon_2(\xi) = 1 + \frac{2}{\pi} \int_0^\infty \frac{\omega \varepsilon_2(\omega)}{\omega^2 + \xi^2} d\omega \quad (3)$$

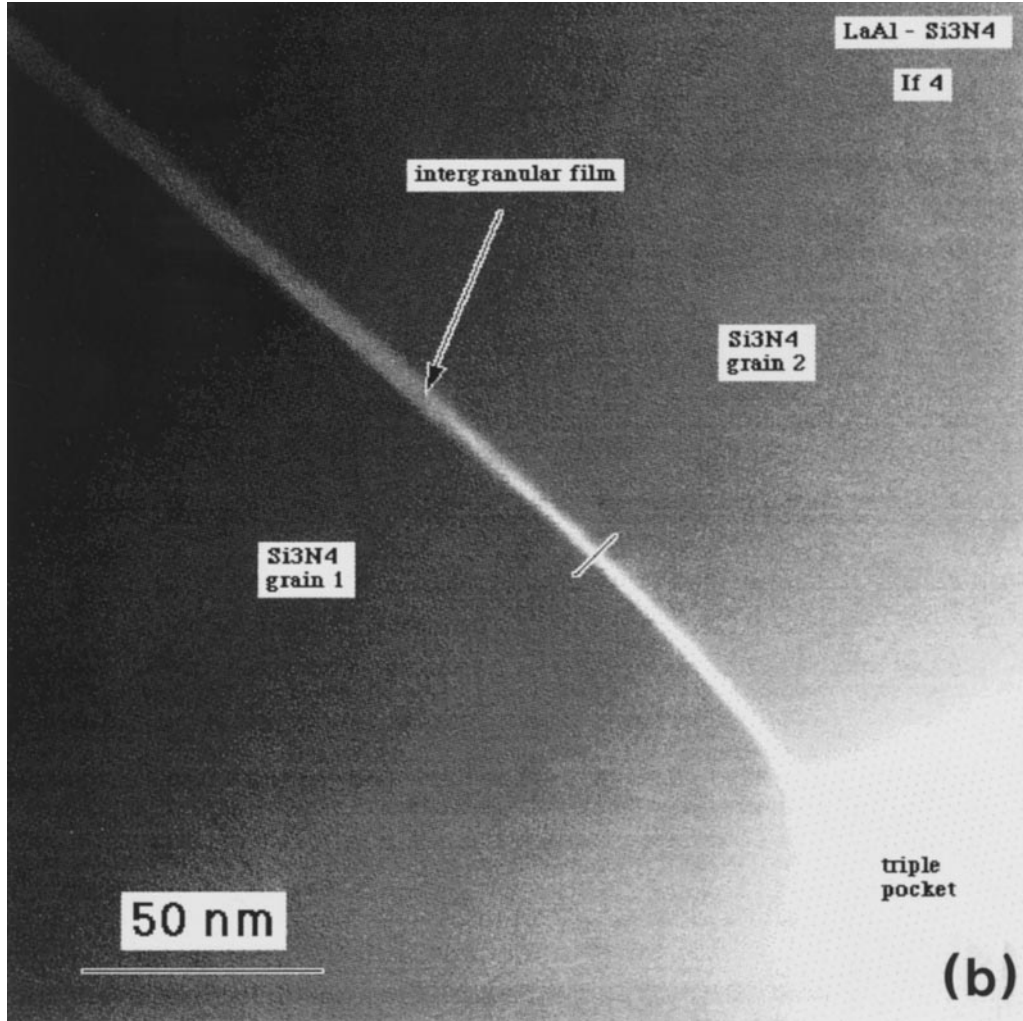


Fig. 3. STEM micrographs of the LaAl-Si<sub>3</sub>N<sub>4</sub> sample showing the four interfaces, (a) IF 1 to IF 3 and (b) IF 4 where SR-VEEL spectrum images were acquired. For IF 4 the 10 nm spectrum image scan line along which the multiplexed SR-VEEL spectrum image was acquired is shown.

to calculate the London dispersion spectrum [59, 60]  $\epsilon_2(\xi)$ , which is an intrinsic physical property of the material. Once the London dispersion spectra are calculated, then particular values of the Hamaker constants for any configuration can be determined using equation (4) by evaluating the integrals of the functions  $G$  (equation (5)) which are simple differences of the London dispersion spectra (equation (6)).

$$A = \frac{-3\sqrt{L}^2}{\pi} \int_0^\infty \rho \, d\rho \int_0^\infty \ln G(\xi) \, d\xi \quad (4)$$

$$G_{121}^{\text{NR}}(\xi) = 1 - \Delta_{12}^2 e^{-2a\rho} \quad (5)$$

$$\Delta_{kj} = \frac{\epsilon_{2,k}(\xi) - \epsilon_{2,j}(\xi)}{\epsilon_{2,k}(\xi) + \epsilon_{2,j}(\xi)} \quad (6)$$

Therefore after the London dispersion spectra  $\epsilon_2(\xi)$  are calculated, they are accumulated in a spectral

database [61] from which any combinations of them can be used to calculate the Hamaker constants of interest. For each VEEL spectrum image, three interband transition strengths were selected, one from each Si<sub>3</sub>N<sub>4</sub> grain and one from the middle of the IGF (Fig. 5). Full spectral Hamaker constants determined from each SR-VEEL spectrum image in each type of Si<sub>3</sub>N<sub>4</sub> material are tabulated in Table 1 for YAl-Si<sub>3</sub>N<sub>4</sub>, in Table 2 for LaAl-Si<sub>3</sub>N<sub>4</sub>, and in Table 3 for Ca-SiO<sub>2</sub>-Si<sub>3</sub>N<sub>4</sub>. The Si<sub>3</sub>N<sub>4</sub>|vacuum|Si<sub>3</sub>N<sub>4</sub> Hamaker constants and the Si<sub>3</sub>N<sub>4</sub>|IGF|Si<sub>3</sub>N<sub>4</sub> Hamaker constants are summarized in Table 4.

### 3.5. Hamaker constants in relation to intergranular film properties

From the full VEEL spectrum images we can extract a number parameters across the IGF. From the ratio of the intensities in the total spectrum to

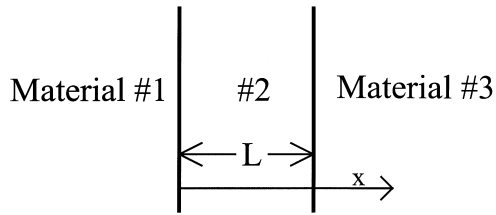


Fig. 4. Configuration of materials for a  $A_{123}$  Hamaker constant where the intervening film is of material #2 and the two adjacent grains are of material #1 and #3. For the simpler case of a  $A_{121}$  or  $A_{1v1}$ , the two grains are considered to be of the same material #1 and the intervening film is of material #2 or of vacuum (v).

the zero loss peak intensity the relative thickness of the specimen can be determined in units of the mean free path [41] (Fig. 6). This clearly reveals the position of the IGF and aids in the selection of the interband transition strength for the calculation of the Hamaker constants.

At the end of the analysis, the index of refraction can be calculated from the dielectric function across the IGF (Fig. 7). Obviously the index for bulk  $\text{Si}_3\text{N}_4$  is recovered, but also the index of refraction for the IGF is obtained by this method. The variations in the index of refraction calculated at the end of the analysis for bulk  $\text{Si}_3\text{N}_4$  in the different materials varies only within the statistical fluctuations, indicating that the analysis is stable and insensitive to numerical inaccuracies. Correspondingly the Hamaker constants for  $[\text{Si}_3\text{N}_4|\text{vacuum}|\text{Si}_3\text{N}_4]$  vary by less than 5%. The

index of refraction for the IGFs (Fig. 8) and the corresponding Hamaker constants (Fig. 9) on the other hand show a clear dependence on the composition of the IGF. When the Hamaker constant is plotted against the IGF index of refraction (Fig. 10) it is observed, that the Hamaker constant decreases almost linearly with increasing index of refraction of the IGF, except for very low Hamaker constants.

From the profiles of the index of refraction across the IGF it is possible to measure a IGF thickness. This will not be identical to the IGF thickness as determined by HREM, but will be related to it. Here it serves as an indication of the variation in IGF thickness between different interfaces. For the LaAl material a clear correlation between this IGF thickness and the Hamaker constant is seen (Fig. 11). This puts the large error bars observed in Fig. 9 into perspective, indicating that it is not statistical fluctuations within the method but rather fluctuations within the microstructure and IGF chemistry. This variation between different interfaces is much larger than the variations arising from the methods, as becomes obvious when the error bars for several measurements on one interface are compared with the scattering between different interfaces (Fig. 12).

### 3.6. Intergranular film composition

It is known that the IGF thickness in silicon nitride depends on the chemistry of the amorphous phase [13, 14, 19, 20]. Therefore it is important to know or determine the IGF chemistry together with the Hamaker constants. For the Ca doped sample

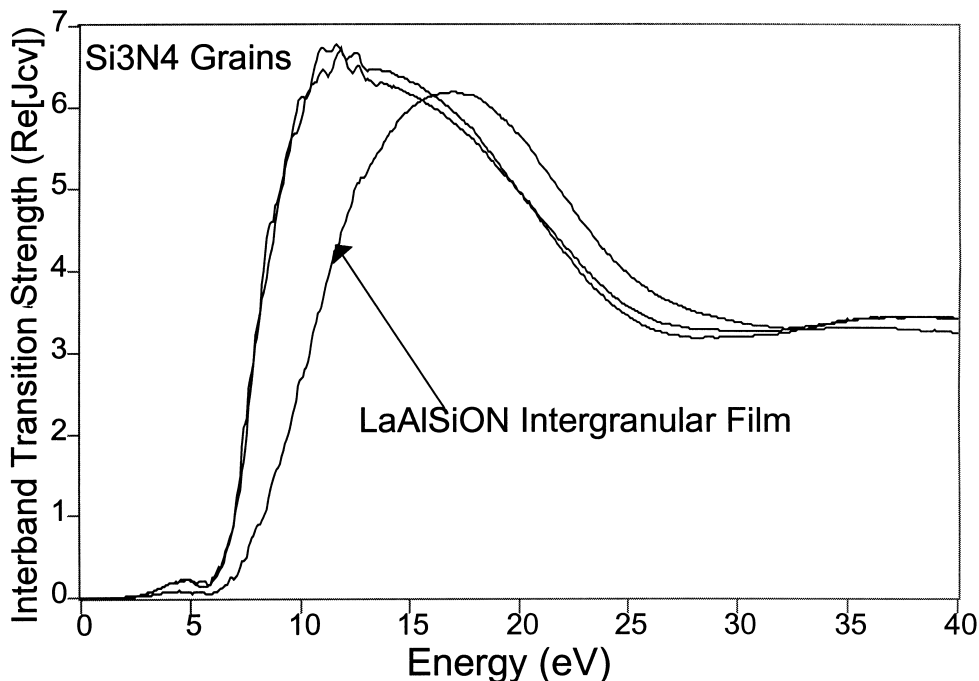


Fig. 5. Interband transition strength spectra for the IGF, and each  $\text{Si}_3\text{N}_4$  grain from La-Al  $\text{Si}_3\text{N}_4$ .

Table 1. Index of refraction and Hamaker constants from analysis of SR-VEEL spectrum images of Si<sub>3</sub>N<sub>4</sub> prepared with a Y–Al–Si–O–N glass

Spec. image/ interface	$n$ (Si <sub>3</sub> N <sub>4</sub> )	$A_{1v1}$ w/vacuum (zJ)	$n$ (IGF)	$A_{121}$ w/IGF (zJ)
z054/IF1	2.02	187.3	1.71	8.63
	1.99	184.1		7.79
z055/IF1	1.95	174.5	1.66	8.30
	1.95	175.1		8.41
z056/IF1	1.94	186.6	1.67	8.84
	1.93	185.3		8.50
z057/IF1	2.00	189.9	1.69	10.00
	1.96	188.0		9.34
Average	1.97	183.8	1.68	8.73
Std. dev.	0.03	5.5	0.02	0.6

Averages are over all spectrum images.

Table 2. Index of refraction and Hamaker constants from analysis of SR-VEEL spectrum images of Si<sub>3</sub>N<sub>4</sub> prepared with a La–Al–Si–O–N glass

Spec. image/ interface	EELS film thickness (nm)	$n$ (Si <sub>3</sub> N <sub>4</sub> )	$A_{1v1}$ w/vacuum (zJ)	$n$ (IGF)	$A_{121}$ w/IGF (zJ)
z059/IF. 1		1.99	177.8	1.72	6.49
		1.96	176.4		6.13
z060/IF. 2	2.17	1.95	168.4	1.84	1.39
		2.04	174.2		2.06
z061/IF. 2	2.06	1.96	169.3	1.80	2.37
		1.95	168.2		2.22
z062/IF. 3	1.86	1.98	175.0	1.75	4.20
		1.95	170.3		3.32
z063/IF. 4	1.45	1.97	175.5	1.58	15.69
		1.97	176.1		15.87
z064/IF. 4		1.89	163.7	1.61	8.81
		1.96	169.6		10.46
z065/IF. 4		1.96	175.4	1.62	12.35
		1.95	174.7		12.10
Average		1.96	172.5	1.70	7.4
Std. dev.		0.03	4	0.09	5

Averages are over all spectrum images.

Table 3. Index of refraction and Hamaker constants from analysis of SR-VEEL spectrum images of Si<sub>3</sub>N<sub>4</sub> prepared with a Ca–Si–O–N glass with 450 ppm Ca

Spec. image/interface	$n$ (Si <sub>3</sub> N <sub>4</sub> )	$A_{1v1}$ w/vacuum (zJ)	$n$ (IGF)	$A_{121}$ w/IGF (zJ)
z047/IF1	1.95	175.2	1.55	18.51
	1.95	173.6		17.94
z048/IF2	1.92	163.2	1.50	20.42
	1.91	161.9		19.90
z049/IF2	1.94	176.2	1.48	26.07
	1.89	174.8		25.25
z050/IF2	2.12	189.8	1.55	24.83
	1.89	173.9		17.41
z051/IF3	1.92	172.1	1.64	9.00
	1.96	177.0		10.33
z053/IF3	2.00	179.8	1.58	18.18
	2.09	188.5		21.44
Average	1.96	175.5	1.55	19.11
Std. dev.	0.07	7.9	0.06	5.1

Averages are over all spectrum images.

Table 4. Index of refraction for Si<sub>3</sub>N<sub>4</sub> and IGFs and Hamaker constant ( $A_{1v1}$ ) for [Si<sub>3</sub>N<sub>4</sub>vacuum]Si<sub>3</sub>N<sub>4</sub>, and Hamaker constant ( $A_{121}$ ) for [Si<sub>3</sub>N<sub>4</sub>]IGF[Si<sub>3</sub>N<sub>4</sub>] configurations

Glass	$d$ (nm)	#	$n$ (Si <sub>3</sub> N <sub>4</sub> )	$A_{1v1}$ (zJ)	$n$ (IGF)	$A_{121}$ (zJ)
Y–Al (VUV)	1.2		1.96 ( )	192.1 ( )	1.77 ( )	9.33 ( )
Y–Al (IF 1)	1.2	4	1.97 (0.03)	183.8 (5.5)	1.68 (0.02)	8.73 (0.6)
La–Al (IF 1)	1.6	1	1.98 ( )	177.1 ( )	1.72 ( )	6.3 ( )
La–Al (IF 2)	1.6	2	1.98 (0.04)	170.0 (2.4)	1.82 (0.02)	2.0 (0.4)
La–Al (IF 3)	1.6	1	1.97 ( )	172.6 ( )	1.75 ( )	3.8 ( )
La–Al (IF 4)	1.6	3	1.95 (0.03)	172.5 (4.5)	1.60 (0.02)	12.6 (2.6)
La–Al (avg.)	1.6		1.97 (0.01)	173.1 (2.6)	1.72 (0.08)	8.3 (4.5)
High Ca (IF 1)	1.45	1	1.95 ( )	174.4 ( )	1.55 ( )	18.2 ( )
High Ca (IF 2)	1.45	3	1.95 (0.08)	173.3 (9.3)	1.49 (0.01)	22.9 (2.8)
High Ca (IF 3)	1.45	2	1.99 (0.06)	179.4 (6.0)	1.59 (0.04)	14.7 (5.2)
High Ca (avg.)	1.45		1.96 (0.02)	175.7 (2.7)	1.54 (0.04)	18.6 (3.4)

Averages are over the interfaces measured.  $d$  is the nominal film thickness, # is the number of spectrum images in the averages, and in the index of refraction and Hamaker constant columns the mean and standard deviations are listed.

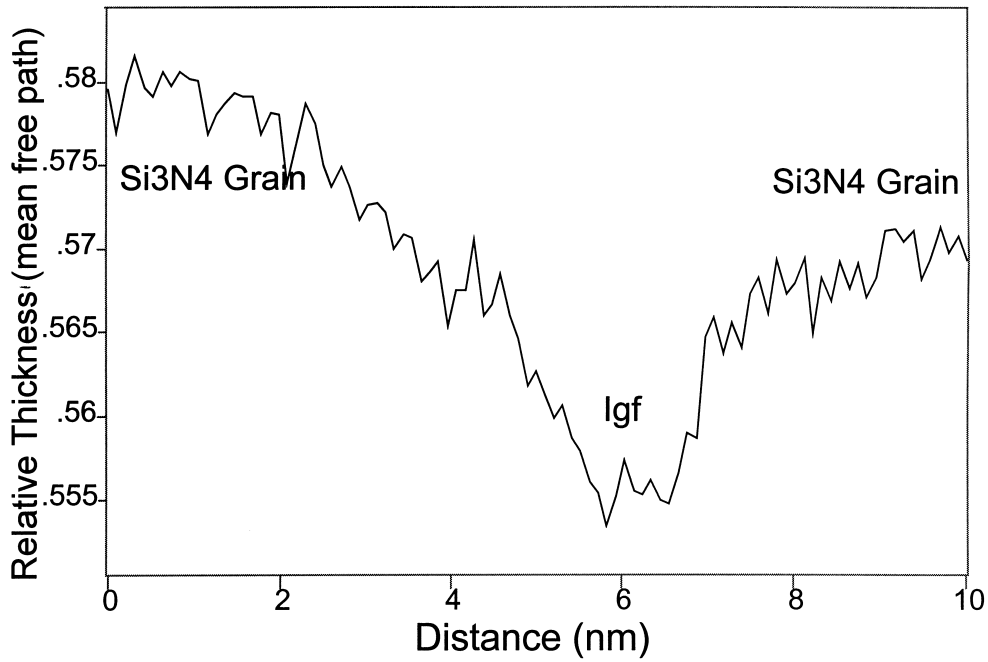


Fig. 6. Relative thickness of the TEM foil sample, in units of electron mean free path, as a function of position across the IGF from La-Al  $\text{Si}_3\text{N}_4$ .

the IGF chemistry has been studied extensively by Gu [15–17]. The material doped with 450 ppm Ca has 2.5 Ca atoms per  $\text{nm}^2$  of interfacial area. For YAl- $\text{Si}_3\text{N}_4$  the chemical composition of a triple point, which was at the end of the investigated

grain boundary, was determined by energy dispersive X-ray spectroscopy (EDS). Quantification of Al, Si and Y showed that the cation composition was 1.1 wt% Al, 25.8 wt% Si and 73.1 wt% Y. For the LaAl sample spectrum images were acquired

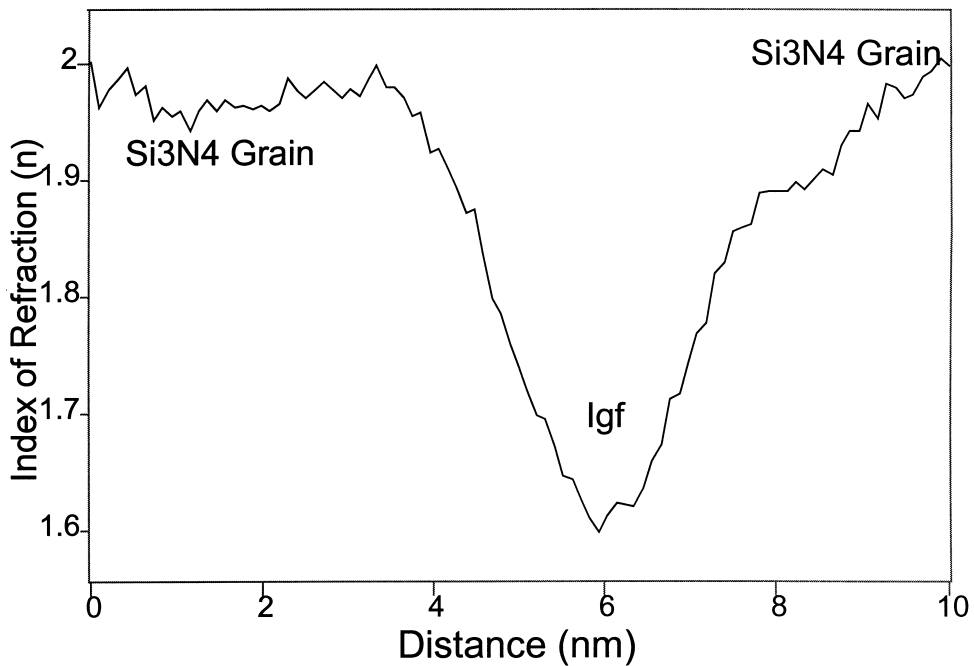


Fig. 7. Index of refraction determined from the index sum rule applied to the interband transition strength spectrum image from La-Al  $\text{Si}_3\text{N}_4$ .

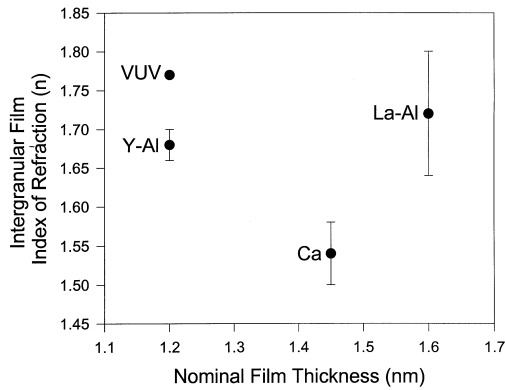


Fig. 8. Index of refraction of the IGFs in the various types of  $\text{Si}_3\text{N}_4$  materials plotted according to nominal IGF thickness reported in HREM. The VUV measurement for Y-Al is from a bulk glass sample of the same nominal composition as the glass phase in  $\text{Si}_3\text{N}_4$ .

with the same hardware as described above but recording the energy loss range including the N and O K-edges as well as the La  $M_{4,5}$ -edge. Quantification of these elemental profiles was performed as described in another paper of this issue [62]. The results are summarized in Table 5.

#### 4. DISCUSSION

Recent work has developed the ability to calculate full spectral Hamaker constants from experimental interband transition strengths. At the same time additional work on the quantitative analysis of SR-VEEL spectra and SR-VEEL spectrum images can now supply the required interband transition strength results for individual IGFs in  $\text{Si}_3\text{N}_4$ . The combination of SR-VEEL spectrum imaging and full spectral Hamaker constants permits the *in situ* determination of vdW forces on the IGFs in silicon nitride based ceramics and also the local variations

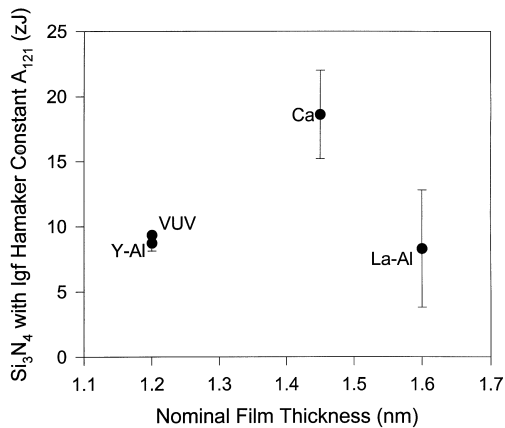


Fig. 9. Hamaker constant  $A_{121}$  for  $[\text{Si}_3\text{N}_4]\text{IGF}[\text{Si}_3\text{N}_4]$  determined for the various types of  $\text{Si}_3\text{N}_4$  materials plotted according to nominal IGF thickness reported in HREM.

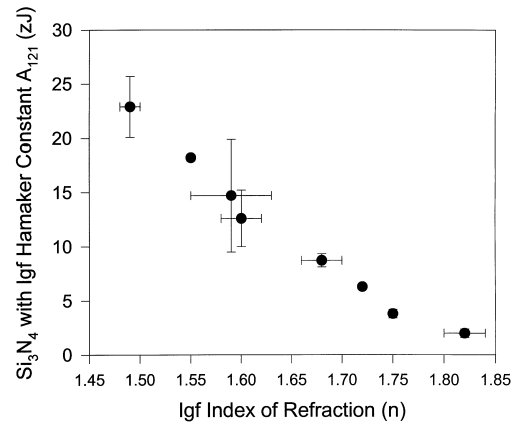


Fig. 10. Hamaker constant  $A_{121}$  as a function of the index of refraction of the IGF for all materials.

in dispersion forces throughout the microstructure of individual silicon nitride samples. This is shown in the present paper, and the results indicate that the uncertainties arising from the analysis are much smaller than the microstructural variations. This becomes most obvious in Fig. 12, where the error bars for the Hamaker constant for each IGF as determined from multiple measurements on the same IGF are considerably smaller than the differences in Hamaker constant for different IGFs. This ability to experimentally determine dispersion forces and Hamaker constants *in situ* represents an important new tool for dispersion force and wetting studies.

The results determined for  $\text{Si}_3\text{N}_4$  and the Y-Al-Si-O-N glass from vacuum ultraviolet spectroscopy (Fig. 2) can be used as reference standards for, and guidance in, our analysis of the SR-VEEL spectra. The VUV results show the volume-averaged index of refraction of the YAl- $\text{Si}_3\text{N}_4$  to be 1.97. This will serve in the present work as the reference value of

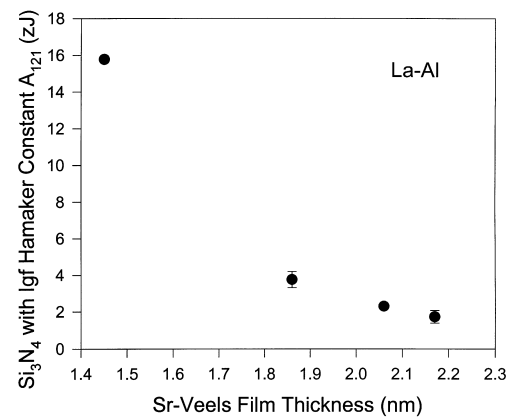


Fig. 11. Hamaker constant  $A_{121}$  for La-Al  $\text{Si}_3\text{N}_4$  material as a function of the IGF thickness as measured from the SR-VEEL index of refraction profiles across the IGF.

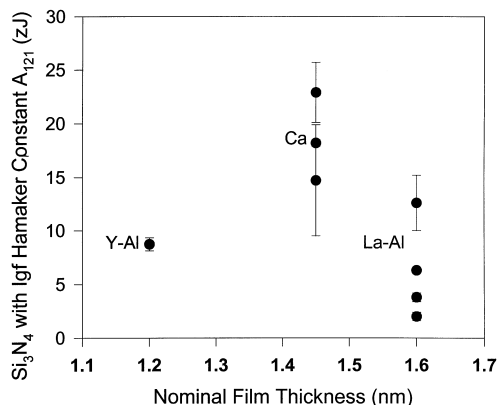


Fig. 12. Hamaker constant  $A_{121}$  for  $[\text{Si}_3\text{N}_4|\text{IGF}|\text{Si}_3\text{N}_4]$  for the various types of  $\text{Si}_3\text{N}_4$  materials plotted according to nominal IGF thickness reported in HREM. The data for each IGF in the different materials are displayed in contrast to Fig. 9 where only the average for each material was shown.

the index of refraction of  $\text{Si}_3\text{N}_4$ . In addition the Hamaker constant  $A$   $[\text{Si}_3\text{N}_4|\text{Vac.}|\text{Si}_3\text{N}_4]$  value of 192 zJ and the  $A$   $[\text{Si}_3\text{N}_4|\text{Y-Al bulk glass}|\text{Si}_3\text{N}_4]$  value of 9.3 zJ will serve as reference values for comparison to the results of SR-VEEL spectrum image analysis.

#### 4.1. SR-VEEL spectrum imaging analysis and dispersion force determination

VEEL spectroscopy is a suitable method to obtain the interband transition strength from ceramic materials and offers the advantage of high spatial resolution when performed in a dedicated STEM [40]. Here we have optimized the spatial resolution to the primary beam diameter, by using the newly developed spectrum imaging hard- and software. This approach results in semi-automatic data acquisition. The advantage is that full information is obtained and that instabilities of the system are either obvious and the data can be discarded or a correction is possible. For the first time it has been possible to acquire two spectra with different exposure times for the same beam location (pixel). The analysis of these data is still complex and consists of several steps. The most crucial ones are the correct splicing of spectra which is made difficult by small energy shifts occurring between the two spectra belonging to one pixel and the single scattering deconvolution with accurate removal of the zero

loss line shape. The currently used analysis software solves the first of these two problems and has an adequate solution for the second. In the future there might be better approaches. Details of the data processing have been discussed elsewhere [63].

One problem which has not been addressed so far is that the inelastic scattering for small energy losses is delocalized. Therefore the spatial resolution of the data is a convolution of the primary beam profile with this delocalization function. Currently this has not been removed in the data analysis. For well defined interface geometries, such as planar infinite interfaces, an analytical expression can be given for the VEEL spectrum as a function of beam position [64]. The expression involves the dielectric functions of the materials on both sides of the interface. The reverse problem, i.e. to find the dielectric functions of the materials involved from a measured profile, is not trivial. It might be impossible to solve for the general case. For a symmetric sandwich layer, i.e. the present case of one material between two grains of another material, the expression will be somewhat simpler. Additionally the dielectric function of the bulk material (silicon nitride) is known from the reference measurements away from the interface. It might then be possible to calculate the contribution of the neighboring bulk material (i.e. geometry) to the spectra measured within the IGF, subtract that contribution and obtain the dielectric function of the IGF. This approach will be followed in the future. For the materials investigated here the IGF widths are all well above 1 nm whereas the beam diameter was only 0.6 nm. The delocalization is expected to be of about 1 nm [65] and was therefore neglected here.

The situation becomes even more complicated if the chemical composition across the IGF is inhomogeneous. This might actually be the case for the Ca doped specimens, where there are several possibilities under discussion [19, 20], namely homogeneous distribution of the cations, accumulation in the middle or at both sides of the IGF. Before such cases can be considered substantial work is required both in chemical analysis at atomic resolution and analysis of the electronic structure from measured VEEL spectrum images.

In this work only three spectra were used to calculate the Hamaker constant, one from each bulk  $\text{Si}_3\text{N}_4$  grain and one of the IGF taken from the middle of the IGF as determined by the minimum

Table 5. IGF chemistry of LaAl- $\text{Si}_3\text{N}_4$

Glass	#	N deficit $\Gamma$ ( $\text{nm}^{-2}$ )	O excess $\Gamma$ ( $\text{nm}^{-2}$ )	La excess $\Gamma$ ( $\text{nm}^{-2}$ )
La-Al (IF 1)	2	31.0 (3.1)	14.1 (2.4)	5.4 (0.6)
La-Al (IF 2)	1	44.9	21.0	9.1
La-Al (IF 3)	3	40.4 (18.9)	32.12 (15.6)	7.9 (2.8)
La-Al (IF 4)	5	57.3 (9.0)	26.4 (4.0)	7.7 (0.9)
La-Al (avg.)		46.8 (14.9)	25.2 (9.8)	7.5 (1.8)

Averages are over the interfaces measured. # is the number of spectrum images in the averages, and in the nitrogen (N), oxygen (O) and lanthanum (La) coverage ( $\Gamma$ ) columns the mean and standard deviations are listed.

in the profile of the index of refraction across the IGF (Fig. 7). Figure 7 also indicates that the variation of the measurement within the bulk material is of the order of 1%. The exact form of the profile across the IGF will depend on two factors. The first is the delocalization discussed above. For the spectrum from the middle of the IGF this effect can be neglected (see discussion above). The second influence is the variation of chemical composition across the IGF which cannot be taken into account in the present analysis. If such variation exists it would influence the Hamaker constant and more sophisticated data analysis schemes will have to be developed to investigate whether this effect is present or not. The advantage of the spectrum imaging method is that the optimum spectrum for the IGF can be picked, which is the one from the middle of the IGF. If only three measurements are performed, one on the IGF and one on each grain, there might be further uncertainties involved such as specimen drift or inaccurate positioning of the beam on the IGF.

#### 4.2. Dispersion forces, Hamaker constants and intergranular film thickness

In pursuing this study of *in situ* dispersion force determination for numerous silicon nitride IGFs using samples from two glass systems (lanthanide doped and calcia doped) with three dopant systems (Y–Al, La–Al and Ca doped glass), many questions about the accuracy of the developed methods needed to be addressed so as to define the accuracy and limitations on our knowledge of these dispersion forces. The determination of dispersion forces by calculation of full spectral Hamaker constants from SR-VEEL spectrum images shows a reproducibility of the Hamaker constant determination of better than 1 zJ standard deviation when multiple measurements are made on individual IGFs, as shown in Table 4. Greater variability in the Hamaker constant as seen in some multiple measurements on a single IGF most probably arise from true variability in the physical properties and composition of this IGF. The accuracy of these methods is demonstrated by the close agreement between the Hamaker constant for  $[\text{Si}_3\text{N}_4|\text{Yal-Si}_3\text{N}_4|\text{Si}_3\text{N}_4]$  determined by SR-VEEL spectrum imaging (8.7 zJ) and determined by VUV spectroscopy of bulk samples (9.3 zJ). (Discrepancies observed in earlier work [47] have been removed by the improved data analysis.) Therefore we can conclude that the methods developed allow us to measure the variability of dispersion forces among samples and among IGFs in single samples. Also the variability of the Hamaker constants of the dispersion forces, when larger than 1 zJ standard deviation, are probably associated with true variability in the dispersion forces arising from physical differences in the IGFs and samples.

From this work it can be seen that the dispersion forces on the IGFs in these types of  $\text{Si}_3\text{N}_4$  vary from 2 to 23 zJ, a factor of greater than 10 in the Hamaker constant, the dispersion force law scaling factor. Previously there may have been speculation that variations in the dispersion force did not play a major role in dictating the force balance. But a variation by a factor of 10 in the dispersion force might well be an important component in the force balance in optimized  $\text{Si}_3\text{N}_4$  materials exhibiting equilibrium IGFs. If the dispersion force is the major attractive force counterbalancing the other repulsive terms, then changes of this magnitude in the attractive term are obviously critical. Alternatively, the dispersion force variation might be swamped by other terms which are of larger absolute magnitude, with the effect that the dispersion force would not play an important role. But the present results discount this idea. From the study of individual IGFs in LaAl– $\text{Si}_3\text{N}_4$  shown in Fig. 11 there is a direct correlation between variations in the dispersion force on the IGF and the measured IGF thickness. This demonstrates that for the optimized  $\text{Si}_3\text{N}_4$  materials studied here, which have been sintered to a final state microstructure and exhibit equilibrium IGFs, a major contributing term in the IGF thickness is the vdW dispersion force on the IGFs.

In light of these findings it is interesting to consider the trends seen among the  $\text{Si}_3\text{N}_4$  materials. Acknowledge that the variability in IGF thickness seen in any one sample can arise for different IGFs in the sample, and these can be caused by physical or compositional variations among the IGFs in the sample. Still among different glass systems, for example the two lanthanide glass systems studied here, in general the La–Al glass exhibits a higher index of refraction than the Y–Al glass system, and this increased index matching of the intergranular glass to the  $\text{Si}_3\text{N}_4$  grains produces a reduction in the dispersion forces and a concomitant thickening of the IGF. Yet the variability of interface IF4 in the La–Al sample still exhibited a larger dispersion forces, and thinner IGF thickness, due to physical or compositional non-uniformity in this sample. Moving to a very different glass system, as represented by the Ca  $\text{Si}_3\text{N}_4$  system, the other terms in the intergranular force, such as the glass viscosity, will be very different, so there is not a direct correlation between the magnitude of the Hamaker constant and the observed IGF thickness. For a common glass system, the magnitude of the Hamaker constant of the dispersion force correlates directly to the observed IGF thickness, while a differing glass system will have different magnitudes for the additional terms in the force balance, which serves to renormalize the relationship between Hamaker constant and IGF thickness.

#### 4.3. Composition of the intergranular glass

To better understand the role of physical or compositional properties of the IGF's on the IGF thickness, direct determination of the IGF compositions and variation would be useful so as to track the cause of the variability between interfaces within one specimen. Does the variability in the Hamaker constants for the IGFs in the LaAl arise from changes in the interfacial chemistry? From our compositional measurements, there seems not to be a direct correlation between Hamaker constants and the IGF chemistry. This might be due to the fact that whereas both were measured on the same interface but not on the same day; there could have been slight differences in specimen tilt and other experimental factors. More importantly consecutive chemistry measurements on one interface showed variability in the determination of the chemistry, which have to be attributed to instabilities of the experimental set-up. For example it was observed that during the acquisition of a spectrum image for the determination of the chemistry, the specimen would jump by distances of the order of 10 nm. While these data sets were not analyzed, similar effects might have occurred on a smaller, and therefore undetected, scale in the other data sets, violating the assumption of linear drift in these data. Previously it has also been noticed that in Si<sub>3</sub>N<sub>4</sub> the grain boundary, i.e. the specimen moves with the beam during the acquisition of these chemistry spectrum images [66], thereby altering the results considerably. Incidentally these drift effects were not observed when the SR-VEEL spectra images analyzed in this paper were acquired.

The major finding of this paper is that the IGF thicknesses in different optimized Si<sub>3</sub>N<sub>4</sub> samples with common glass systems correlate very closely to the magnitudes of the Hamaker constants of, and dispersion forces at, the IGFs. Unfortunately the *in situ* chemical composition determinations for these IGFs are not reproducible enough in these measurements to answer the next question. Is the main cause of the changes in the Hamaker constants and IGF dispersion forces arising from changes in the chemical composition of the IGF, or from other electronic and atomic structural changes in the intergranular glass? This question will have to be left for further investigation.

#### 5. CONCLUSIONS

The Hamaker constants representing the van der Waals dispersion forces were determined from *in situ* SR-VEEL spectroscopy for three different IGF chemistries in silicon nitride material. Full profiles from one silicon nitride grain across the amorphous IGF into the grain on the other side were acquired with a new spectrum image acquisition system. The full data set was analyzed and the interband tran-

sition strength determined as a function of beam position. From those data the Hamaker constant was calculated for the actual interface investigated based on spectra from the center of the IGF. The method proved to be accurate and reproducibly with comparison to VUV measurements for the bulk materials and repeated measurements on numerous individual IGFs. These showed standard deviations on the order of 1 zJ for systems with IGFs. For different glass additives having different film thickness, the accurate Hamaker constants provide a basis to calculate the first of the terms in the controlling force balance. Local variations in Hamaker constants within the microstructure of a single sample correlate inversely to the distribution of IGF thickness observed. For these optimized Si<sub>3</sub>N<sub>4</sub> materials, the dispersion forces varied over a range from 2 to 12 zJ, corresponding to a 50% increase of the IGF thickness. This ability to experimentally determine Hamaker constants *in situ* represents an important new tool for dispersion force and wetting studies.

*Acknowledgements*—The authors would like to acknowledge M. Hoffmann for the LaAl and YAl Si<sub>3</sub>N<sub>4</sub> samples and I. Tanaka for the SiO<sub>2</sub>-Si<sub>3</sub>N<sub>4</sub> samples. The assistance of M. Sycha with TEM specimen preparation and C. Scheu, A. D. Dorneich and S. Loughin in the spectroscopy and L. K. DeNoyer in the analysis was also essential. One of us (H. M.) acknowledges financial support of the Volkswagen Stiftung (contract I/70082).

#### REFERENCES

- Clarke, D. R. and Thomas, G., *J. Am. Ceram. Soc.*, 1977, **60**, 491.
- Lou, L. K. V., Mitchell, T. E. and Heuer, A. H., *J. Am. Ceram. Soc.*, 1978, **61**, 392.
- Simpson, Y. K., Carter, C. B., Morrissey, K. J., Angelini, P. and Bentley, J., *J. Mater. Sci.*, 1986, **21**, 2689.
- Flaitz, P. L. and Pask, J. A., *J. Am. Ceram. Soc.*, 1987, **70**, 449.
- Shaw, T. M. and Duncombe, P. R., *J. Am. Ceram. Soc.*, 1991, **74**, 2495.
- Rühle, M., Claussen, N. and Heuer, A. H., *Adv. Ceram.*, 1984, **12**, 352.
- Olsson, E. and Dunlop, G. L., *J. Appl. Phys.*, 1989, **66**, 4317.
- Kingery, W. D., in *Ceramic Microstructures '86: Role of Interfaces*, ed. J. A. Pask and A. G. Evans. Plenum Press, NY, 1987, pp. 281.
- Fujimoto, M. and Kingery, W. D., *J. Am. Ceram. Soc.*, 1985, **68**, 169.
- Callahan, D. L. and Thomas, G., *J. Am. Ceram. Soc.*, 1990, **73**, 2167.
- Chiang, Y. M., Silverman, L. E., French, R. H. and Cannon, R. M., *J. Am. Ceram. Soc.*, 1994, **77**, 1143.
- Lange, F. F. and Clarke, D. R., *J. Am. Ceram. Soc.*, 1982, **65**, 502.
- Kleebe, H.-J., Cinibulk, M. K., Tanaka, I., Bruley, J., Cannon, R. M., Clarke, D. R., Hoffman, M. J. and Rühle, M., *Mater. Res. Soc. Symp. Proc.*, 1993, **287**, 65.
- Kleebe, H.-J., Cinibulk, M. K., Cannon, R. M. and Rühle, M., *J. Am. Ceram. Soc.*, 1993, **76**, 1969.

15. Gu, H., Cannon, R. M., Rühle, M., *J. Mater. Res.*, in press.
16. Gu, H., Pan, X., Cannon, R. M., Rühle, M., *J. Am. Ceram. Soc.*, submitted.
17. Gu, H., Rühle, M., *Mater. Res. Soc. Symp. Proc.*, 1996, submitted.
18. Pan, X., Gu, H., Werner, R. V., Danforth, S. C., Cannon, R. M. and Rühle, M., *J. Am. Ceram. Soc.*, 1996, **79**, 2313.
19. Tanaka, I., Bruley, J., Gu, H., Hoffmann, M. J., Kleebe, H. J., Cannon, R. M., Clarke, D. R., Rühle, M., in *Tailoring of Mechanical Properties of Si<sub>3</sub>N<sub>4</sub> Ceramics*. Kluwer Academic Publishers, Stuttgart, 1994, pp. 275.
20. Tanaka, I., Kleebe, H. J., Cinibulk, M. K., Bruley, J., Clarke, D. R. and Rühle, M., *J. Am. Ceram. Soc.*, 1994, **77**, 911.
21. Clarke, D. R., *J. Am. Ceram. Soc.*, 1987, **70**, 15.
22. Wang, C.-M., Pan, X., Hoffman, M. J., Cannon, R. M. and Rühle, M., *J. Am. Ceram. Soc.*, 1996, **79**, 788.
23. Clarke, D. R., Shaw, T. M., Philipse, A. and Horn, R. G., *J. Am. Ceram. Soc.*, 1994, **76**, 1201.
24. French, R. H., Cannon, R. M., DeNoyer, L. K. and Chiang, Y.-M., *Solid State Ionics*, 1995, **75**, 13.
25. Argento, C. and French, R. H., *J. Appl. Phys.*, 1996, **80**, 6081.
26. Ackler, H. D., French, R. H. and Chiang, Y. M., *J. Colloid Interface Sci.*, 1996, **179**, 460.
27. Ren, S.-Y. and Ching, W. Y., *Phys. Rev. B*, 1981, **23**, 5454.
28. Robertson, J., *Philos. Mag. B*, 1981, **44**, 215.
29. Sokel, R. J., *J. Phys. Chem. Sol.*, 1980, **41**, 899.
30. Ching, W. Y. and Ren, S. Y., *Phys. Rev. B*, 1981, **24**, 5788.
31. Xu, Y.-N. and Ching, W. Y., *Phys. Rev. B*, 1995, **51**, 17379.
32. Morosanu, C.-E., *Thin Solid Films*, 1980, **65**, 171.
33. Bulkin, P. V., Smart, P. L. and Lacquet, B. M., *Opt. Eng.*, 1994, **33**, 2894.
34. Mashita, M., Matsushima, K., *Jpn. J. Appl. Phys. Suppl. 2*, Pt. 1, 1974, 761.
35. Livengood, R. E., Petrich, M. A., Hess, D. W. and Reimer, J. A., *J. Appl. Phys.*, 1988, **63**, 2651.
36. Petalas, J. and Logothetidis, S., *Phys. Rev. B*, 1994, **50**, 11801.
37. Loughin, S., French, R. H., DeNoyer, L. K., Ching, W.-Y. and Xu, Y.-N., *J. Phys. D*, 1996, **29**, 1740.
38. French, R. H., *J. Am. Ceram. Soc.*, 1990, **73**(3), 477.
39. Johs, B., French, R. H., Kalk, F. D., McGahan, W. A. and Woollam, J. A., *Opt. Interference Coat. SPIE*, 1994, **2253**, 1098.
40. Müllejjans, H. and French, R. H., *J. Phys. D*, 1996, **29**, 1751.
41. Egerton, R. F., *Electron energy-loss spectroscopy in the electron microscope*, 2nd ed. Plenum Press, New York, 1996, p. 485.
42. Howie, A. and Milne, R. H., *Ultramicroscopy*, 1985, **18**, 427.
43. Walls, M. G., *Electron Energy-loss Spectroscopy of Surfaces and Interfaces*, Ph.D. Thesis, University of Cambridge, 1987.
44. Walsh, C. A., *Modeling and Interpretation of Electron Energy-loss Spectra from Interfaces* Ph.D. Thesis, University of Cambridge, 1989.
45. Hunt, J. A. and Williams, D. B., *Ultramicroscopy*, 1991, **38**, 47.
46. Colliex, C., Tencé, M., Lefèvre, E., Mory, C., Gu, H., Bouchet, D. and Jeanguillaume, C., *Mikrochem. Acta*, 1994, **114/115**, 71.
47. French, R. H., Scheu, C., Duscher, G., Müllejjans, H., Hoffmann, M. J., Cannon, R. M., *Proceedings of the Symposium on Structure and Properties of Interfaces in Ceramics*, ed. D. Bonnell, U. Chowdhry, M. Rühle, Materials Research Society, 1995, pp. 243.
48. UBE Industries, Ltd., Ube, Yamaguchi 755, Japan.
49. Krämer, M., Hoffman, M. J. and Petzow, G., *J. Am. Ceram. Soc.*, 1993, **76**, 2278.
50. Kramers, H. A., *Atti Congr. Int. Fis. Como.*, 1927, **2**, 545.
51. Kronig, R., *J. Opt. Soc. Am.*, 1926, **12**, 547.
52. Bortz, M. L. and French, R. H., *Appl. Spectrosc.*, 1989, **43**(8), 1498.
53. Gatan Software EI/P v. 3.0, Gatan Inc., Pleasanton, CA.
54. Hamaker, H. C., *Physica*, 1937, **4**(10), 1058.
55. Lifshitz, E. M., *Sov. Phys. JETP*, 1956, **2**, 73.
56. Dzyaloshinskii, I. E., Lifshitz, E. M. and Pitaevskii, L. P., *Adv. Phys.*, 1961, **10**(38), 165.
57. Ninham, B. W. and Parsegian, V. A., *J. Chem. Phys.*, 1970, **52**, 4578.
58. Hough, D. B. and White, L. R., *Adv. Colloid Interface Sci.*, 1980, **14**, 3.
59. London, F., *Trans. Faraday Soc.*, 1937, **33**, 8.
60. London, F., *Z. Phys. Chem. B*, 1936, **11**, 246.
61. Hamaker.ab, v. 3.6, a component of Electronic Structure Tools, Spectrum Square Associates, 755 Snyder Hill Road, Ithaca, NY 14850, U.S.A.
62. Müllejjans, H., unpublished results.
63. Dorneich, A. D., French, R. H., Müllejjans, H., Loughin, S., Rühle, M., *J. Microsc.*, submitted.
64. Howie, A. and Milne, R. H., *Ultramicroscopy*, 1985, **18**, 427.
65. Ritchie, R. H., Howie, A., Echenique, P. M., Besbas, G. L., Ferrell, F. L., Ashley, J. C., in *Fundamental Electron and Ion Beam Interactions with Solids for Microscopy, Microanalysis and Microlithography*, ed. J. Schou, P. Kruit and D. E. Newbury, 1990, pp. 45.
66. Gu, H., private communication.
67. Duscher, G., Müllejjans, H., Rühle, M., unpublished results.
68. Veels.ab, v. 6.9, Kkeels.ab v. 7.5, components of Electronic Structure Tools, Spectrum Square Associates, 755 Snyder Hill Road, Ithaca, NY 14850, U.S.A., which run under GRAMS/32, Galactic Industries, 325 Main Street, Salem, NH 03079, U.S.A.

APPENDIX A

SR-VEEL Spectrum Imaging

To detect subtle changes at the interface, we step the beam along a line across the interface as shown in the micrograph of interface (IF) 4 in the LaAl-Si<sub>3</sub>N<sub>4</sub> sample (Fig. 3), while recording a VEEL spectrum at each pixel so as to acquire a one-dimensional SR-VEEL spectrum image. In addition to improve upon the 14 bit accuracy of the Gatan 666 system, we multiplexed the spectra, whereby two spectra with different integration times are acquired at each image pixel, as shown by the timing diagram in Fig. A1. These multiplexed one dimensional spectrum images were made possible by hardware additions to the GATAN Digiscan, a digital beam control, and a newly developed extensive software package [67] implemented within the GATAN EI/P software. The first spectrum contains an unsaturated, optimized zero loss peak, while the second spectrum at the same pixel is a plasmon optimized spectrum, i.e. with the plasmon peak near to, but below, saturation. The intensity between the two spectra is varied by exposing the specimen to the primary electron beam for varying times and blanking it in between. The spatial resolution of this method is equal to the primary electron beam diameter. The signal-to-noise ratio for each pixel is improved considerably because the unsaturated parts with high counting statistic of the two

spectra are combined. Instabilities of the microscope, especially specimen drift, can be determined by observing the image before and after the spectrum image acquisition. This effect can be removed from the data set by assuming a constant drift velocity. Beam damage is minimized as the specimen is only exposed to the primary electron beam during data acquisition and blanked otherwise. Typical data sets contain two times 100 spectra acquired along a line of 10 (20) nm length, which result in an optimized SR-VEEL spectrum image with a spectrum spacing of 0.1 (0.2) nm. This spacing between pixel is several times smaller than the beam width and therefore an over sampling is achieved.

The analysis of the SR-VEEL spectrum images, including dark current, gain, and single scattering correction were performed using Veels.ab [68] and are discussed in greater detail by Dorneich [63]. A typical multiplexed SR-VEEL spectrum image, acquired across an IGF in the LaAl-Si<sub>3</sub>N<sub>4</sub> material is shown in Fig. A2. Initially the multiplexed zero loss optimized (zlo) and plasmon optimized (plo) spectrum must be fitted and spliced together. This is done in an automated routine, where the two spectra at each pixel are scaled and energy shifted (in quantities less than the interchannel energy difference) so as to minimize the chi squared deviation between the zlo and plo spectra. The multiple scattering (MS), which can be seen at twice the plasmon energy, or approximately 50 eV in Fig. A2, is

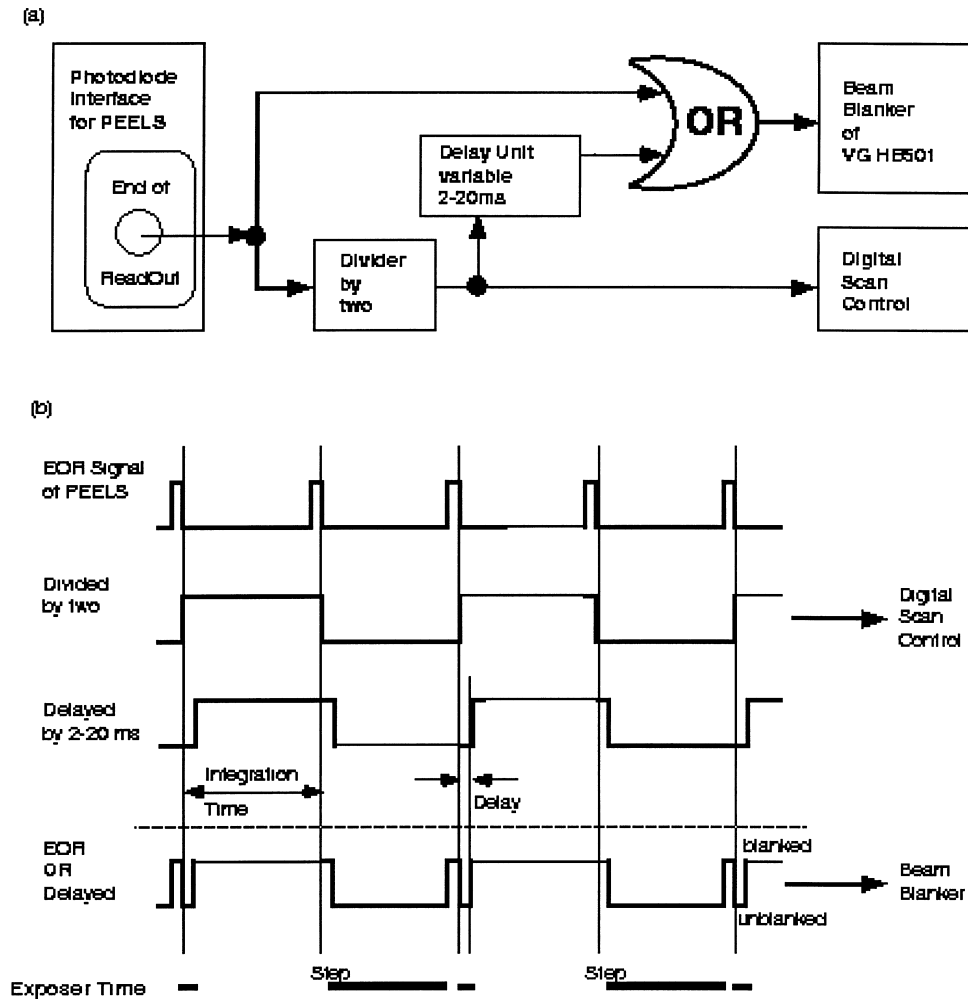


Fig. A1. Digital timing circuit and diagram of the multiplexing method used to acquire zero loss/plasmon loss optimized SR-VEEL spectrum images.

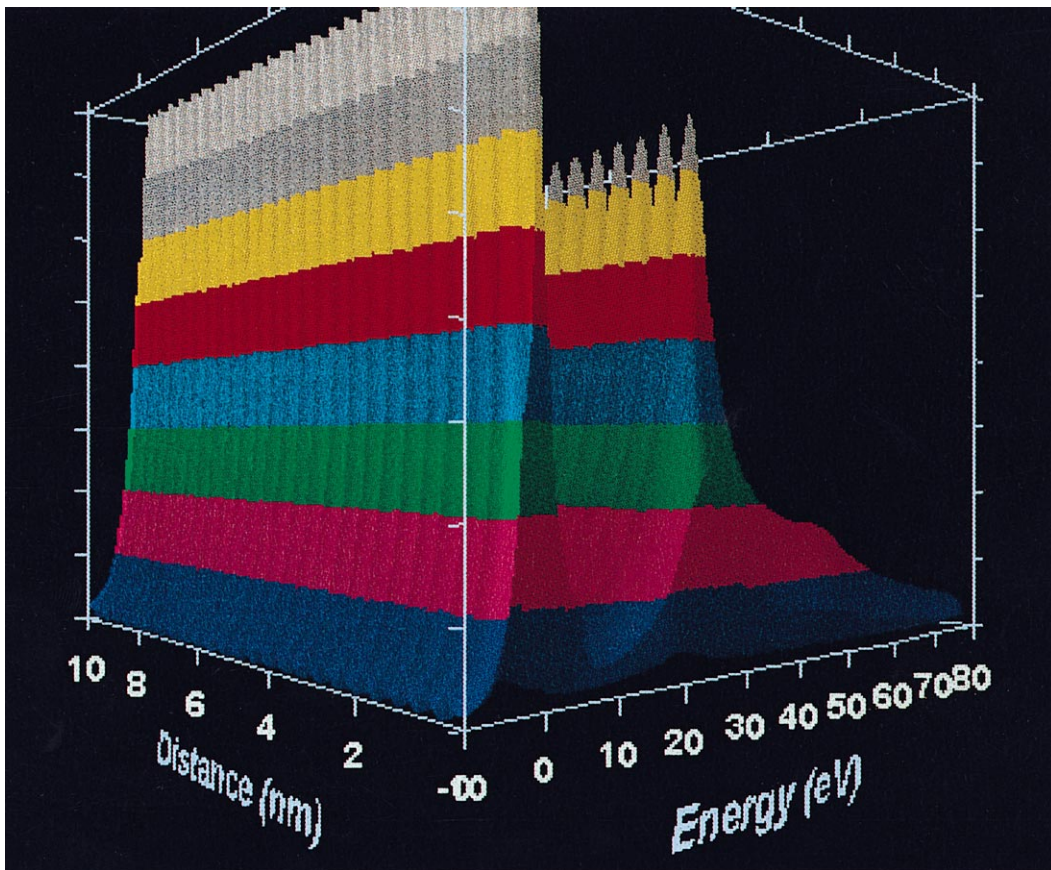


Fig. A2. SR-VEEL multiplexed spectrum image taken in the  $\text{LaAl-Si}_3\text{N}_4$  sample across an IGF. The individual zero loss and plasmon loss optimized spectra, taken at each pixel are seen. The length of the spectrum image is 10 nm

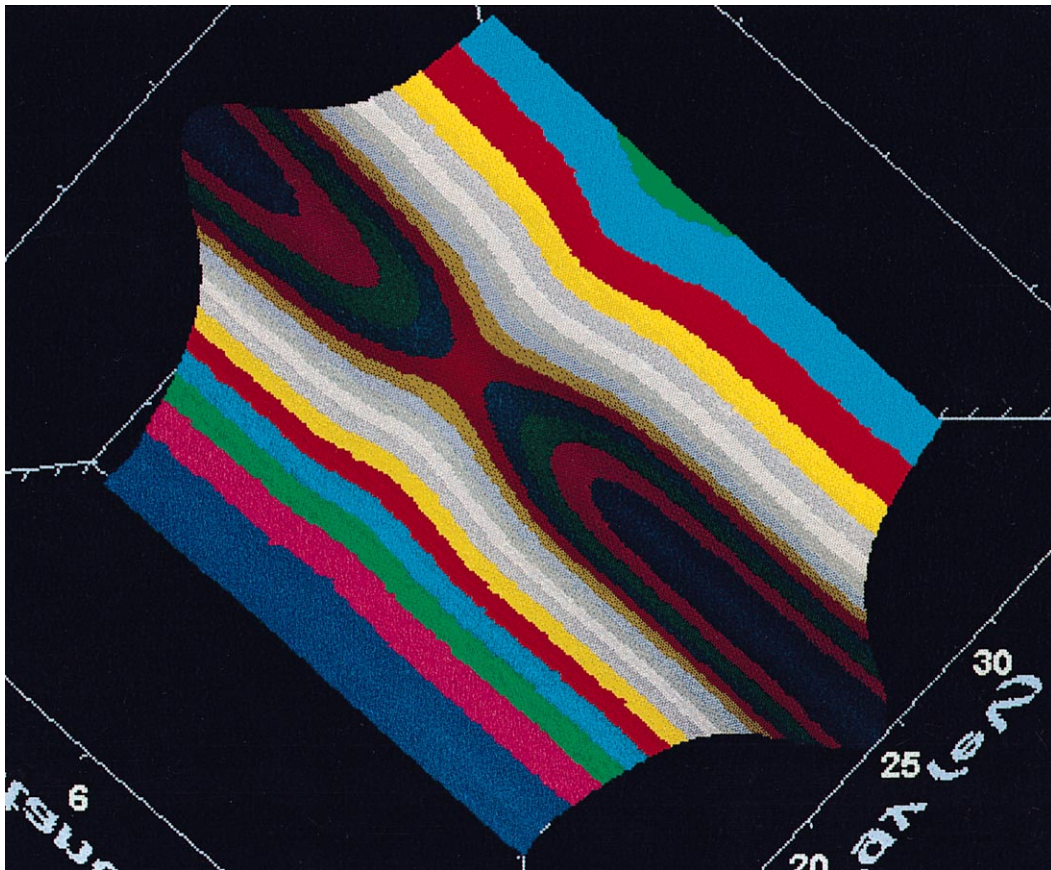


Fig. A3. Single scattering energy loss function spectrum image across an IGF in the  $\text{LaAl-Si}_3\text{N}_4$  sample. The length of the spectrum image is 10 nm. The point of view is looking down on the plasmon peak, with increasing energy loss on the right hand axis, and distance on the left hand axis.

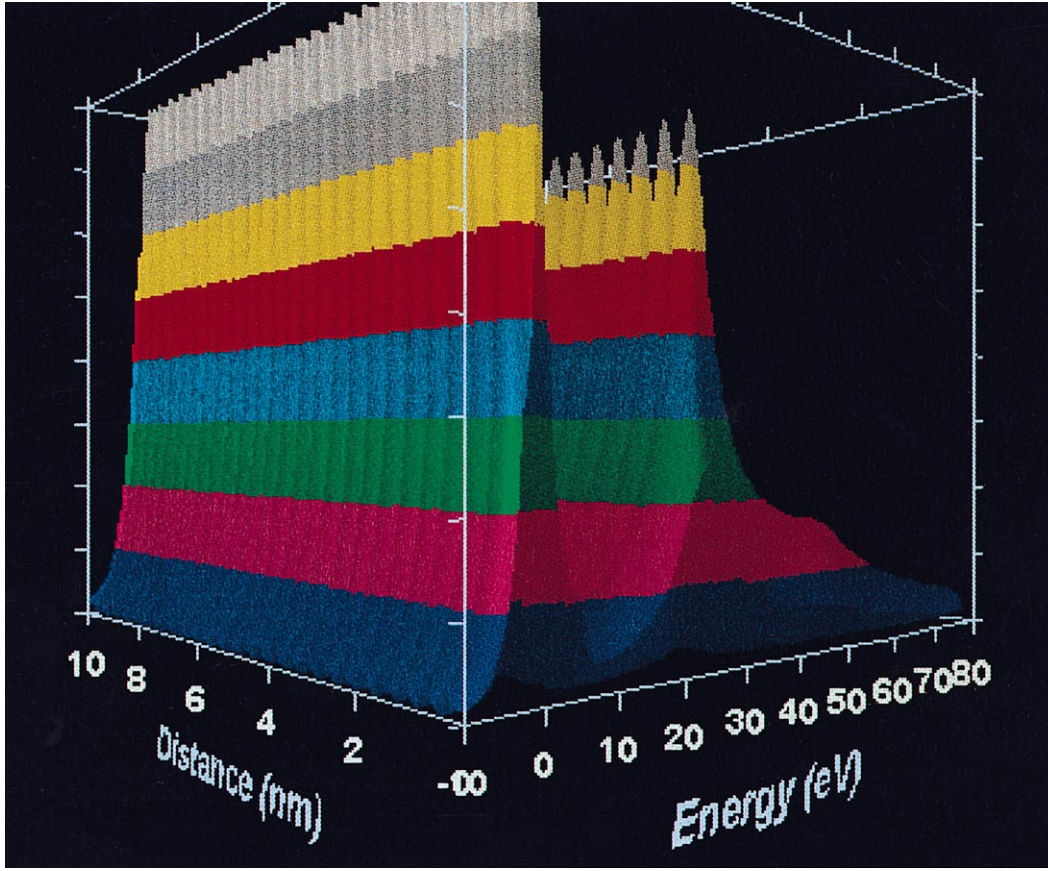


Fig. A4. Interband transition strength ( $\text{Re}[J_{cv}]$ ) spectrum image across an IGF in the  $\text{LaAl-Si}_3\text{N}_4$  sample. The increase in the band gap energy upon entering the IGF is easily seen, as is the shift of the interband transitions to higher energies in the IGF. The right hand axis is energy loss in eV and the left hand axis is distance, where the length of the spectrum image is 10 nm.

then removed using a Fourier-log deconvolution technique to arrive at the single scattering energy loss function. This single scattering correction is one of the most critical steps in the quantitative analysis of SR-VEEL spectra and depends crucially on an accurate knowledge of the zero-loss peak. We use a asymmetric Pearson 7 (aP7) line shape given in equation (7) which is an analytical line shape which can vary from Lorentzian to Gaussian and has well diagonalized parameters permitting rapid fitting. It can also represent a supra-Lorentzian (very wide wings) and supra-Gaussian (very narrow wings) lineshapes.

$$\text{aP7}(E) = H \frac{1}{(1 + 4(x - C)^2 (2^{1/(A(1+P))} - 1)/W^2)^{A(1+P)}} \quad \text{for } x \leq C$$

$$\text{aP7}(E) = H \frac{1}{(1 + 4(x - C)^2 (2^{1/(A(1-P))} - 1)/W^2)^{A(1-P)}} \quad \text{for } x > C \quad (7)$$

Where  $C$  is the peak center,  $H$  is the peak height, and  $W$  is the full width at half-maximum. The parameter  $A$  governs the peak shape and can vary from 0.5 to  $\infty$ .  $A = 1$  corresponds to a pure Lorentzian while  $A = \infty$  corresponds to a Gaussian lineshape. The parameter  $P$  governs the asymmetry and can vary from  $-2000$  to  $+2000$ , with  $P = 0$  corresponding to a symmetric Pearson 7 lineshape. The aP7 is fitted into the zero loss peak, on both the posi-

tive and negative energy loss side, from the energy of the half maximum of the peak to the negative energy end of the data, and on the positive energy loss side up to an energy of typically 4 eV for large band gap materials such as  $\text{Si}_3\text{N}_4$ . Then the calculated aP7 peak shape is used to extend the experimental zero loss data above 4 eV. The resulting single scattering bulk energy loss function spectrum image resulting from this analysis is shown in Fig. A3 for an IGF in the  $\text{LaAl-Si}_3\text{N}_4$  sample. The absolute scaling of the energy loss function is achieved with the index sum rule scaling [63]. We used the index of refraction determined by the optical spectroscopy for bulk  $\text{Si}_3\text{N}_4$ . The scaling factor was then calculated for several VEEL spectra of bulk  $\text{Si}_3\text{N}_4$  on both sides of the IGF at the beginning and the end of the VEEL spectrum image. A linear interpolation between these two regions was used to determine the scaling factor for each single spectrum. This is necessary, since the index of refraction of the IGF is not known and cannot be determined by optical spectroscopy. Once the single scattering energy loss function has been determined then another Kramers Kronig transform [63], equation (8), can be used to calculate the real part of the energy loss function

$$\text{Re}\left[\frac{1}{\hat{\epsilon}(E)}\right] = 1 - \frac{2}{\pi} P \int_0^{\infty} \text{Im}\left[\frac{-1}{\hat{\epsilon}(E')}\right] \frac{E' dE'}{E'^2 - E^2} \quad (8)$$

from its imaginary part. The interband transition strengths and their variation with position in the sample can then be calculated, as shown in Fig. A4 for the  $\text{LaAl-Si}_3\text{N}_4$  sample.